Article

Morphology and Structure of Electrolytically Synthesized Tin Dendritic Nanostructures

Nebojša D. Nikolić [1],*, Jelena D. Lović [1], Vesna M. Maksimović [2] and Predrag M. Živković [3]

1   Department of Electrochemistry, Institute of Chemistry, Technology and Metallurgy, University of Belgrade, Njegoševa 12, 11000 Belgrade, Serbia; jelena.lovic@ihtm.bg.ac.rs
2   Vinča Institute of Nuclear Science—National Institute of the Republic of Serbia, University of Belgrade, 11000 Belgrade, Serbia; vesnam@vin.bg.ac.rs
3   Faculty of Technology and Metallurgy, University of Belgrade, Karnegijeva 4, 11000 Belgrade, Serbia; peca@tmf.bg.ac.rs
*   Correspondence: nnikolic@ihtm.bg.ac.rs; Tel.: +381-11-337-0390

Abstract: The formation of tin dendritic nanostructures by electrolysis from the alkaline electrolyte has been investigated. Morphology and structure of Sn dendrites produced applying both potentiostatic and galvanostatic regimes of the electrolysis are characterized by SEM and XRD, respectively. Depending on the applied cathodic potentials, three types of Sn dendrites were obtained: (a) needle-like and spear-like, (b) fern-like, and (c) stem-like dendrites. The very branchy dendrites with branches of the prismatic shape obtained by the galvanostatic regime of electrolysis represented a novel type of Sn dendrites, not previously reported in the literature. To explain the formation of various dendritic forms, correlation with the polarization characteristics for this electrodeposition system is considered. The needle-like and the spear-like dendrites represented monocrystals of (200),(400) preferred orientation, the fern-like dendrites exhibited the predominant (220),(440) preferred orientation, while in the stem-like particles Sn crystallites were oriented to a greater extent in the (440) crystal plane than in other planes. The galvanostatically synthesized Sn particles possessed the strong (200),(400) preferred orientation. The strong influence of parameters and regimes of electrodeposition on structural characteristics of Sn dendrites is explained by the fundamental laws of electrocrystallization taking into consideration the concept of slow-growing and fast-growing crystal planes.

Keywords: electrodeposition; tin; morphology; structure; dendrite; SEM; XRD

1. Introduction

Thanks to the unique properties of Sn as a metal related to its high electrical conductivity, low electrochemical migration behavior, excellent solderability and low material cost, Sn in the form of powder found wide application in many industries [1]. The most important industries using Sn powder are: powder metallurgy, lithium-ion battery production, electronic industry and manufacture of tin solder paste [2]. Sn powders are also widely used in optoelectronics, production of specialized alloys with copper (bronze), niobium (Nb_3Sn) and zirconium, in production of food packaging for distilled water, beer and carbonated drinks, storage tanks for pharmaceutical chemical solutions, in capacitors electrodes, fuse-wires, ammunitions, tinned iron sheets to protect victuals, sweets, or tobacco, etc. [1]. All these applications make Sn one of the most often used materials globally.

Various methods, such as atomization [1,3], chemical reduction [1,4,5], cementation [1], various polyol [6,7], galvanic displacement [8] and electrochemical deposition [9–11] processes, are used for the synthesis of tin powder particles. The morphology of the particles strongly depends on the method used for their synthesis. For example, Sn nanorods are obtained by polyol process combined with the sonochemical method [7]. The spherical shapes of particles were obtained by reduction process [4] and modified polyol process [6]. The

centrifugal atomization process gave particles of lognormal bell shape [3]. The dendritic particles are the most often shapes obtained by electrochemical deposition processes [9,10]. The dendritic particles can also be obtained by galvanic replacement process [8].

Electrodeposition is a widely applied method for the synthesis of Sn powder particles. This method is a relatively cheap and environmentally friendly way of forming metal powders of high purity of controllable shape and size of particles [12]. It is achieved by the application of various regimes of electrolysis including the application of both constant (potentiostatic and galvanostatic) and periodically changing (pulsating overpotential, pulsating, and reversing current) regimes [13]. The shape and size of the particles also depend on electrolysis parameters, such as the type and composition of electrolyte, current density and cathodic potential applied, time of electrodeposition, temperature and stirring of electrolyte, the type of cathodic material, etc. [13]. Of course, all these regimes and parameters of electrolysis affect the shape and size of Sn powder particles.

Sn and Sn alloys in the powder form can be obtained by electrolysis from the aqueous [9,10,14–22] and non-aqueous electrolytes [23,24], deep eutectic solvent (DES) [2,11,25–27] and ionic liquids [28–31]. Various acidic and alkaline aqueous electrolytes, such as chloride [16], chloride–gluconate [14,15], sulfate–coumarin [10], chloride–citrate [16], chloride–sulfate–gluconate [15], sulfate [17–20] and hydroxide [9] electrolytes are used for a production of tin powders of different surface morphology. The dendrites of various degrees of ramification were obtained from acidic sulfate [17], sulfate with an addition of coumarin [10], chloride with an addition of gluconate [14], and alkaline hydroxide [9] electrolytes. The regular and irregular crystal grains from polyhedral to flaky were obtained from chloride–gluconate and chloride–sulfate–gluconate [15] electrolytes, as well as from chloride–citrate [16] electrolytes. The spongy particles are obtained from the chloride electrolyte [16], while the nanowires were synthesized from non–aqueous dichloromethane-based electrolytes [24]. The 3D foam or the honeycomb-like structures formed under parallel vigorous hydrogen evolution with dendritic branches are obtained by electrolysis from the sulfate electrolytes [17,18]. Depending on the electrolysis conditions, Sn particles with pyramid chain and dendrite structures, and tower cone-shaped and pagoda-shaped morphology are prepared by electrodeposition in choline chlorideethylene glycol deep eutectic solvent (ChCl-EG DES) [2,11].

Anyway, existing investigations of the production of Sn in the powdered forms by electrolysis processes are insufficient and unsystematic. One of the reasons is a lack of correlation between polarization characteristics and morphology of the powder particles formed under various electrolysis conditions. Namely, the polarization characteristics represent the "identity card" of every electrodeposition system and its knowledge is essential in the understanding the mechanism of the formation of metal powders. For that reason, the aim of this study is to correlate the polarization characteristics for Sn electrodeposition from the alkaline hydroxide electrolyte with the morphology of powder particles produced under various electrolysis conditions. Simultaneously, a correlation between morphological and structural characteristics of the powder particles will also be considered.

2. Materials and Methods

2.1. Electrochemical Experiments

Electrodeposition of tin was performed from an electrolyte containing 20 g/L $SnCl_2 \times 2H_2O$ in 250 g/L NaOH at a temperature of $22.0 \pm 0.50\,°C$ by use of constant regimes of electrodeposition. In the potentiostatic regime, electrodeposition was performed at the following cathodic potentials (*E*): −1185, −1200, −1270, −1400, −1600 and −1800 mV vs. Ag/AgCl. The current density (*j*) of −3 mA cm^{-2} was used for electrodeposition in the galvanostatic regime of electrodeposition. The polarization curve for Sn electrodeposition from the same electrolyte was recorded at the scan rate of 1 mV s^{-1}. The polarization curves were also recorded in a blank electrolyte without Sn(II) ions, i.e., in 250 g/L NaOH at the same scan rate.

Sn electrodeposition was performed in the three-compartment cell using BioLogic SP 200 potentiostat/galvanostat. Sn was electrodeposited on copper working electrode of cylindrical shape with the overall surface area of 0.25 cm^2 (length: 1.0 cm; diameter: 0.080 cm). Pt wire was used as the counter electrode, while Ag/AgCl/3.5 M KCl (in the further text, this electrode is denoted as Ag/AgCl) was used as the reference electrode. Electrodeposition of Sn was performed with an amount of electricity of 400 mC. The polarization curve for Sn electrodeposition is recorded on Cu electrode, while those in the blank electrolyte were recorded on Cu and Sn electrodes. Sn electrode was obtained by electrodeposition of Sn on Cu electrode at a cathodic potential of −1180 mV vs. Ag/AgCl with an amount of the electricity of 100 mC. These electrodeposition conditions enabled the formation of uniform Sn film on the Cu electrode.

Before the electrodeposition process, the cylindrical Cu electrodes were firstly decreased at a temperature of 70 °C in alkaline detergent, and then etched in 20% H_2SO_4 at 50 °C. After each phase, the Cu electrodes were rinsed with distilled water. For a preparation of the electrolyte, high purity water (Millipore, 18 M ohm cm resistivity; Merck KGaA, Darmstadt, Germany) and analytical grade reagents were used.

2.2. Characterization of Electrochemically Produced Tin Deposits

Morphology of potentiostatically and galvanostatically electrodeposited tin deposits was characterized by scanning electron microscope (SEM)—model JEOL JSM-6610LV (JEOL Ltd., Tokyo, Japan).

The crystal structure of electrolytically produced tin particles was examined by XRD (X-ray diffraction) method using Rigaku Ultima IV diffractometer, Japan with CuKα radiation. For those purposes, Sn particles were obtained by removing of the deposits from the electrode surface area after finished electrodeposition processes at cathodic potentials of −1200, −1400 and −1800 mV vs. Ag/AgCl, and at a current density of −3 mA cm^{-2}. The XRD analysis of the particles was performed in 2θ range between 20 and 100°. The preferred orientation of synthesized particles was estimated by application of methodology based on a determination of "Texture coefficients" (*TC*(*hkl*)) and "Relative texture coefficients" (*RTC*(*hkl*)) from the XRD data [32–35]. The procedure of determination of these coefficients is presented in Appendix A. The average crystallite size was calculated based on the full-width at half-maximum intensity (FWHM) of all recorded reflections of Sn by applying Scherrer's formula using the PDXL2 software (version 2.0.3.0), with reference to the patterns of the International Centre for Diffraction Database (ICDD), version 2012 [36].

3. Results

3.1. Polarization Characteristics of Sn Electrodeposition Processes

The polarization curve for tin electrodeposition from the alkaline electrolyte is shown in Figure 1a. At the first sight, it can be mentioned that it consists of three parts, as follows:

Part (I)—this part is characterized by the fast increase of the current density and by its sharp decrease after reaching maximum at a cathodic potential of −1185 mV vs. Ag/AgCl,

Part (II)—this part is characterized by a relatively short plateau of the limiting diffusion current density between −1220 and −1320 mV vs. Ag/AgCl. The beginning of the fast increase of the current density with increasing cathodic potential is also attributed to this part, and

Part (III)—this part is characterized by the fast increase in the current density with the increase of cathodic potential.

The boundaries among these parts are denoted by vertical lines in Figure 1a.

Polarization curves recorded in 250 g/L NaOH (the blank electrolyte) on Sn and Cu electrodes are shown in Figure 1b,c, respectively. The recorded curves corresponded to hydrogen evolution reaction, and comparing their shapes it follows that hydrogen evolution commences at more positive potential on Sn relative to Cu electrodes. This clear indicates about lower overpotential for hydrogen evolution reaction on Sn than on Cu electrode. The obtained results were in a line with those reported by Rudnik and Włoch [14].

Also, it follows from Figure 1b,c that hydrogen evolution was more intensive on Cu than on Sn electrodes. These shapes of the polarization curves can also be attributed to the so-called "the electrode effect" [37]. Namely, generated hydrogen bubbles are attached to the cathode surface, so that hydrogen evolution becomes the rate-limiting step of the electrochemical process.

(a)

(b)

(c)
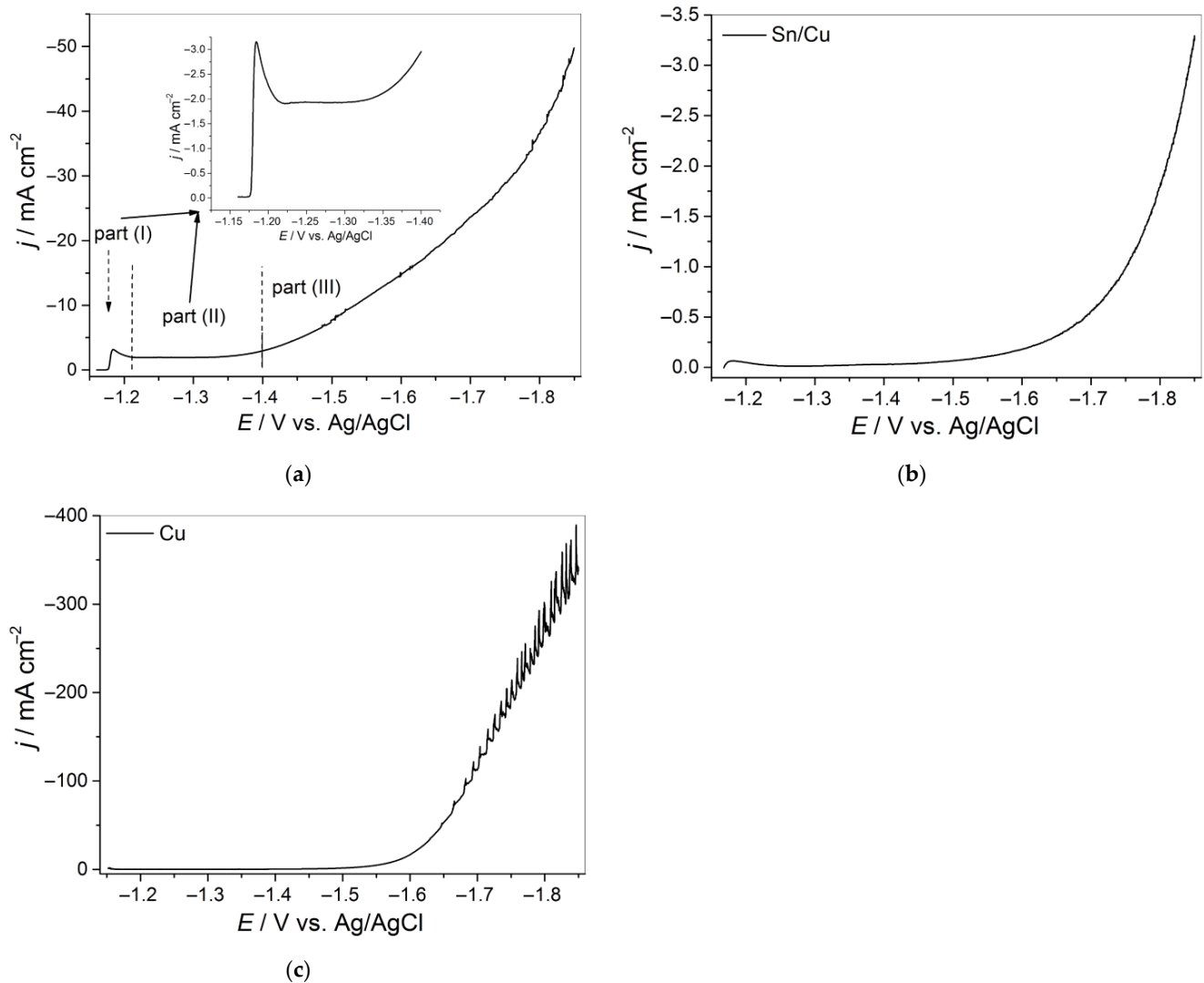
Figure 1. (**a**) Polarization curve for tin electrodeposition from 20 g/L $SnCl_2 \times 2H_2O$ in 250 g/L NaOH recorded on Cu electrode, and polarization curves recorded in electrolyte without Sn(II) ions (the blank electrolyte) on: (**b**) Sn, and (**c**) Cu electrodes; $v = 1$ mV s^{-1}.

Figure 2 shows the chronoamperometric curves recorded on two cathodic potentials from each of these parts: $E = -1185$ and -1200 mV vs. Ag/AgCl for Part (I) (Figure 2a), $E = -1270$ and -1400 mV vs. Ag/AgCl for Part (II) (Figure 2b), and $E = -1600$ and -1800 mV vs. Ag/AgCl for Part (III) (Figure 2c). The common characteristic for all these dependencies is the increase in the current density after certain electrodeposition time, with a tendency to shorten this time with the increase of the cathodic potential applied. The increase in the current density after a certain time of electrodeposition is a clear indicator of the formation and growth of dendrites at these cathodic potentials [38]. In the potentiostatic regime of electrodeposition, the current density rises with the electrodeposition time because the real current density remains constant, while the electrode surface area increases with time [39].
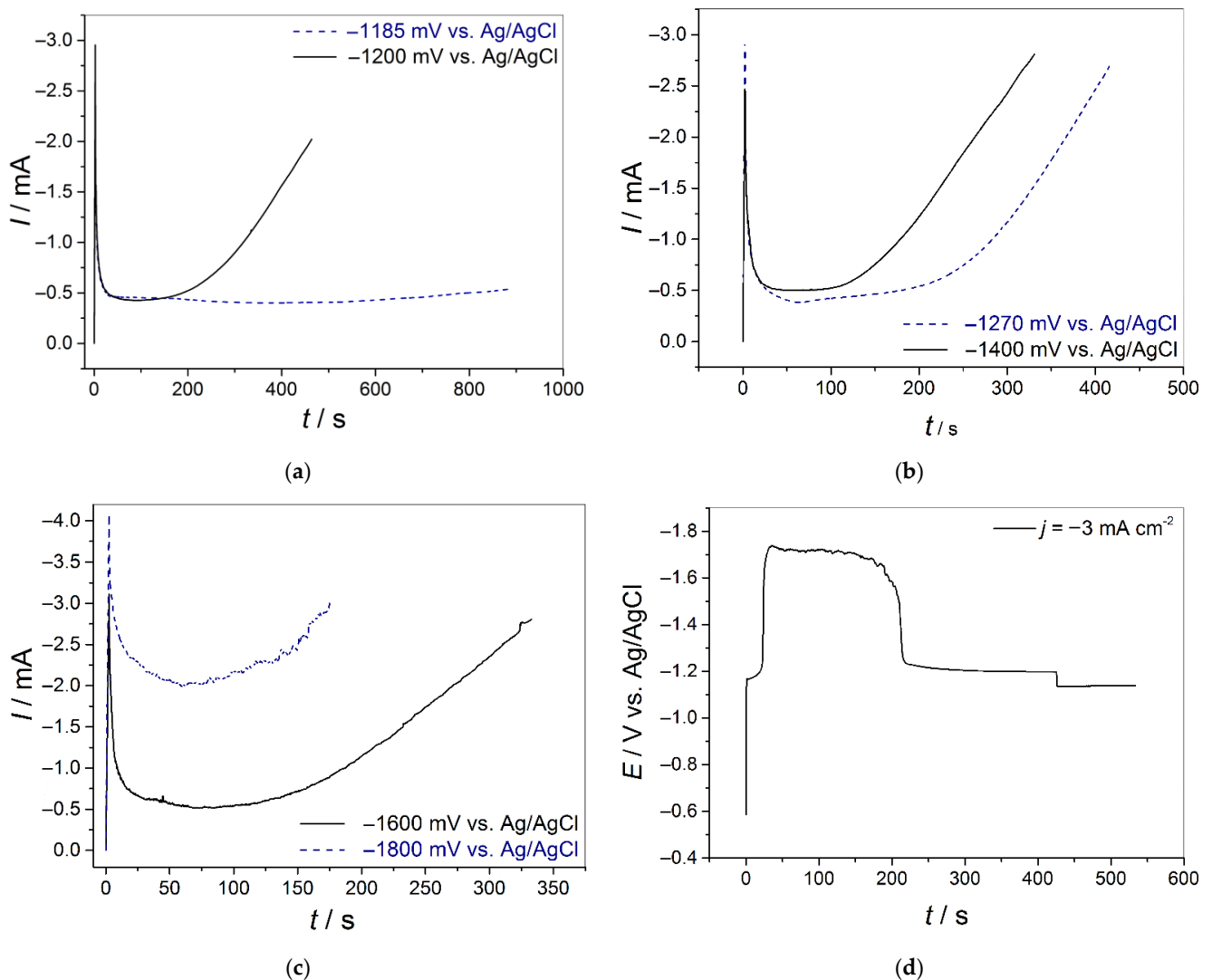
Figure 2. The chronoamperometric curves recorded on cathodic potentials of: (**a**) $E = -1185$ and -1200 mV vs. Ag/AgCl, (**b**) $E = -1270$ and -1400 mV vs. Ag/AgCl, and (**c**) $E = -1600$ and -1800 mV vs. Ag/AgCl, and (**d**) The chronopotentiometric curve recorded at a current density of $j = -3$ mA cm^{-2}. The electrolyte: 20 g/L SnCl$_2 \times 2$H$_2$O in 250 g/L NaOH. The surface area of Cu electrode: 0.25 cm^2.

The chronopotentiometric curve recorded at a current density outside the plateau of the limiting diffusion current density ($j = -3$ mA cm^{-2}) is shown in Figure 2d. The almost three plateaus of the cathodic potentials independent of the electrodeposition time are mentioned from this E–t dependency. The decrease of the cathodic potential with the electrodeposition time is a result of the increase of the electrode surface area, and hence, the decrease of the real current density with time [39].

3.2. Morphology of Sn Deposits Obtained by Potentiostatic and Galvanostatic Regimes of the Electrodeposition

Morphologies of tin deposits obtained at various cathodic potentials from each of the mentioned parts are shown in Figures 3–5.
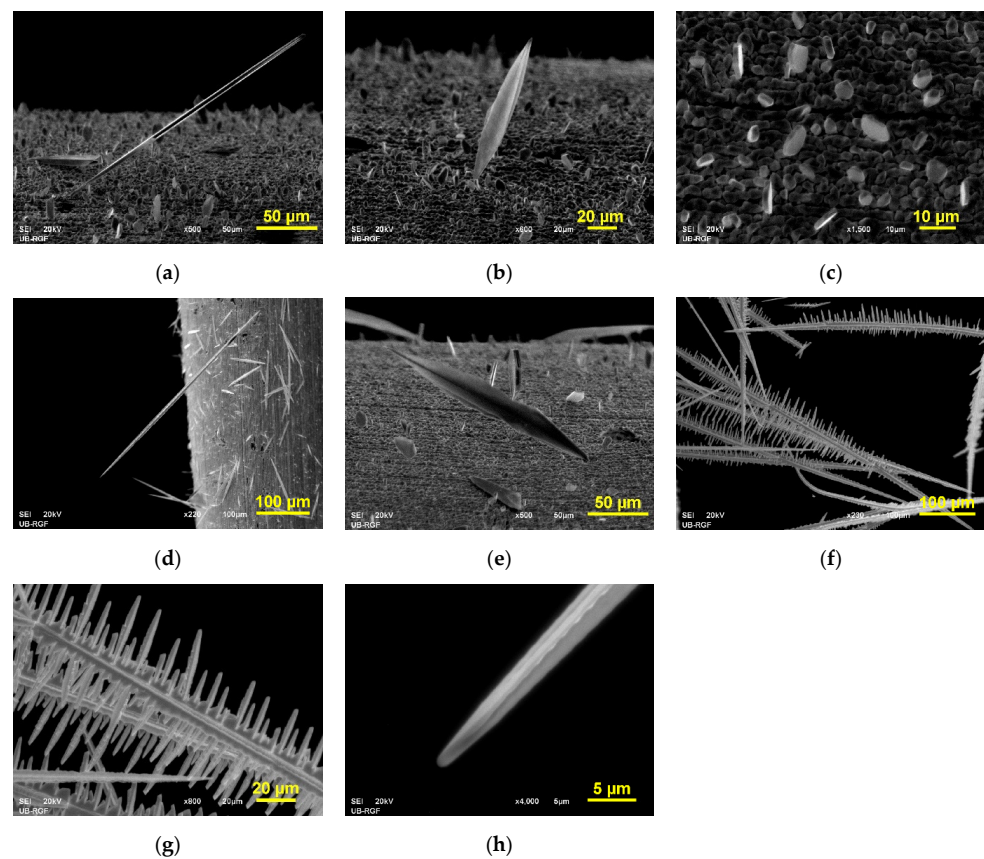
Figure 3. Morphologies of tin deposits electrodeposited at cathodic potentials (*E*) of: (**a–c**) −1185 mV vs. Ag/AgCl, and (**d–h**) −1200 mV vs. Ag/AgCl. The amount of passed electricity: 400 mC.
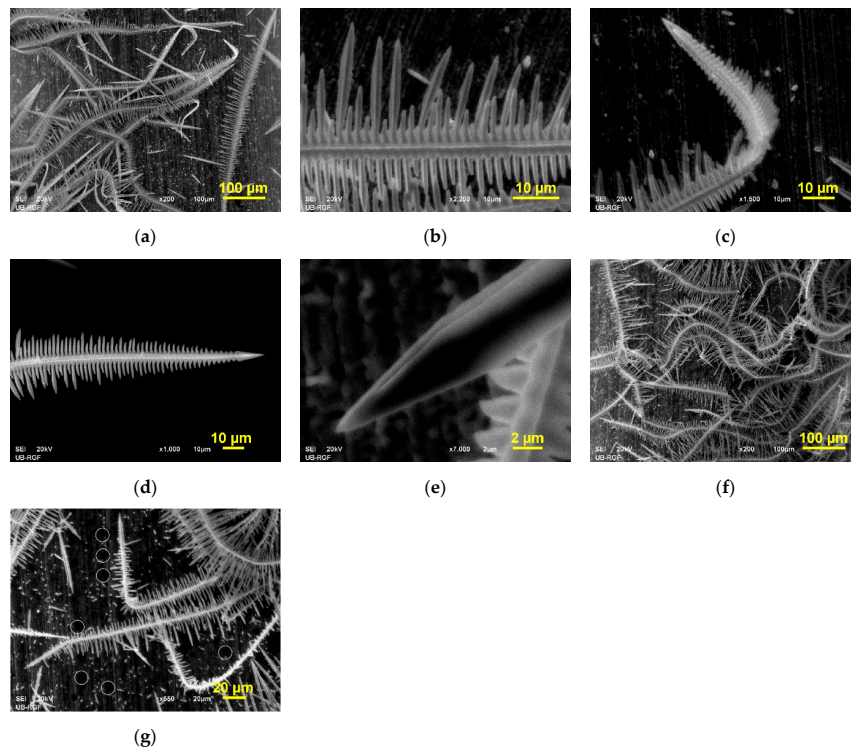
Figure 4. Morphologies of tin deposits electrodeposited at cathodic potentials (*E*) of: (**a–e**) −1270 mV vs. Ag/AgCl, and (**f,g**) −1400 mV vs. Ag/AgCl. The amount of passed electricity: 400 mC.
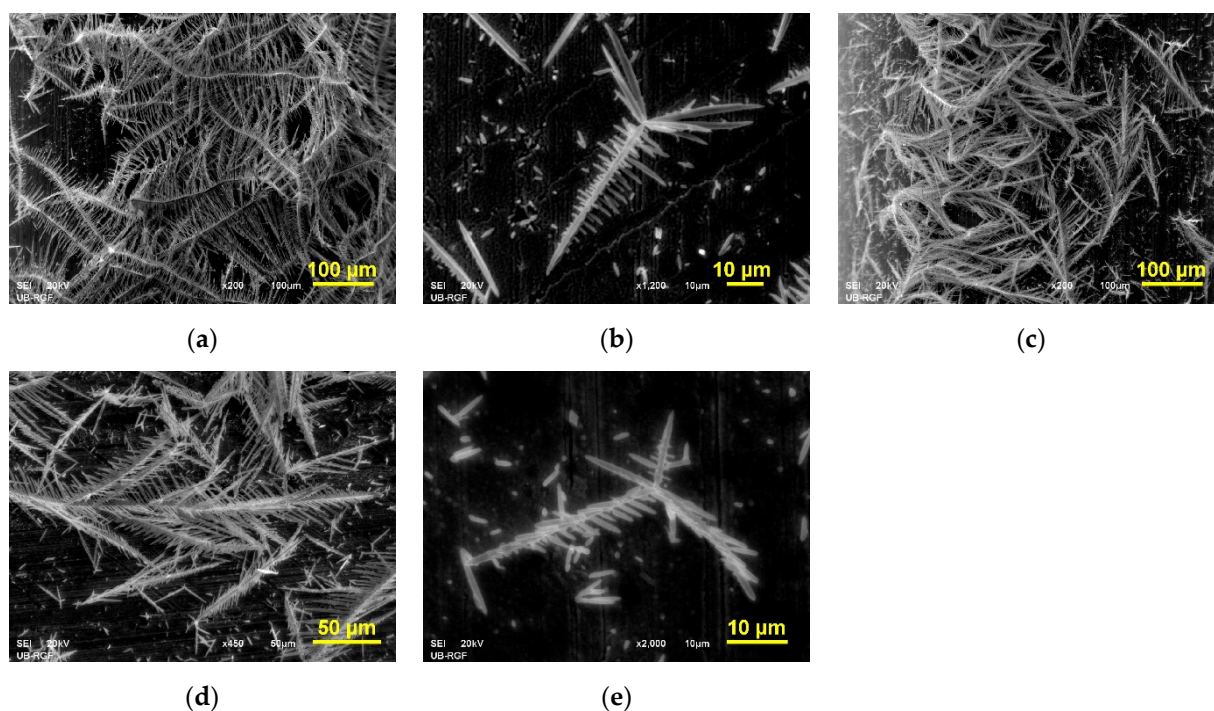
Figure 5. Morphologies of tin deposits electrodeposited at cathodic potentials (*E*) of: (**a**,**b**) −1600 mV vs. Ag/AgCl, and (**c**–**e**) −1800 mV vs. Ag/AgCl. The amount of passed electricity: 400 mC.

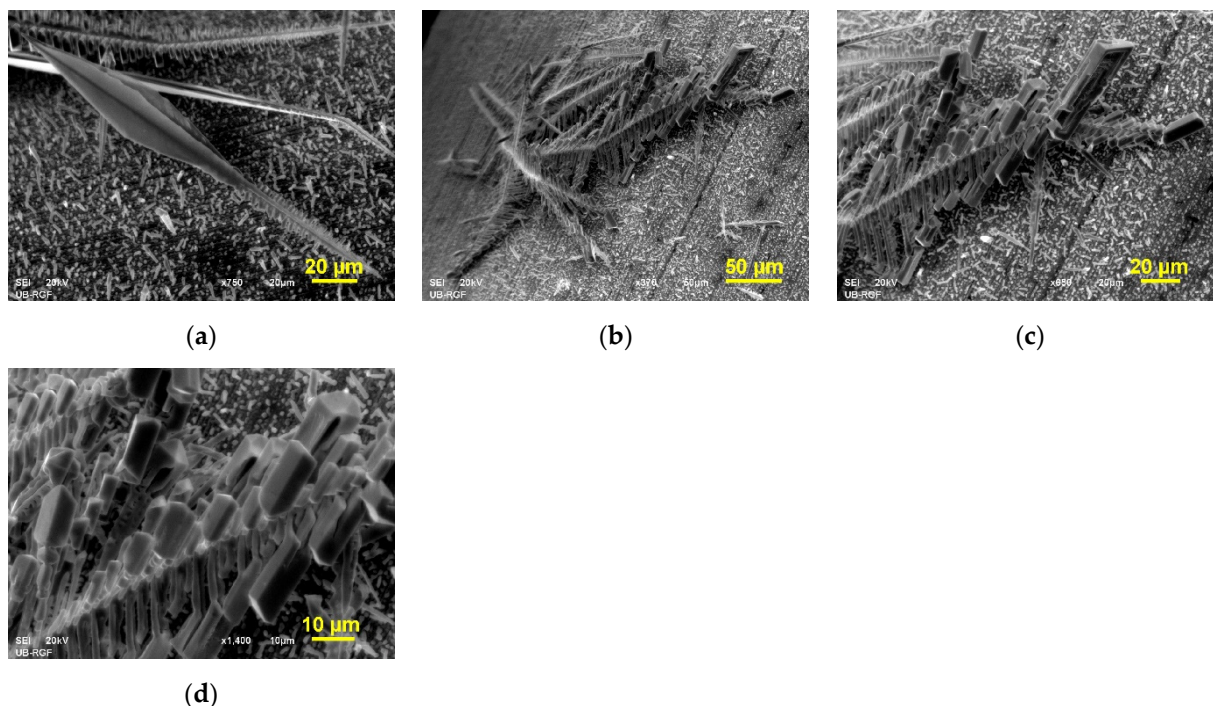Morphologies of Sn deposits electrodeposited at cathodic potentials belonging to maximum at the polarization curve (*E* = −1185 mV vs. Ag/AgCl) and to the descending part of it (*E* = −1200 mV vs. Ag/AgCl) (Part (I) at the polarization curve) are shown in Figure 3. The thin needle-like (Figure 3a) and the spear-like (Figure 3b) dendrites, as well as well-defined crystal grains (Figure 3c) were formed at *E* of −1185 mV vs. Ag/AgCl. The length of the thin needles was approximately up to 250 μm. The thin needle-like dendrites whose length reached up to 300 μm (Figure 3d) and the spear-like dendrites (Figure 3e) were also predominantly formed at *E* of −1200 mV vs. Ag/AgCl. However, aside from these shapes, the needles with developed side branches were also formed (Figure 3f). This shape of the needle-like dendrites had an appearance like fish bone (Figure 3g). Both needle-like and spear-like dendrites formed at both cathodic potentials were oriented by the tips towards the bulk of electrolyte. The tip of one typical needle is shown in Figure 3h.

Figure 4 shows Sn deposits electrodeposited at cathodic potentials situated in the middle of the plateau of the limiting diffusion current density (*E* = −1270 mV vs. Ag/AgCl; Figure 4a–e), and for 80 mV outside the plateau of the limiting diffusion current density (*E* = −1400 mV vs. Ag/AgCl; Figure 4f,g) (Part (II) at the polarization curve). The shape of dendrites formed at these cathodic potentials differed from those obtained at the cathodic potentials belonging to Part (I) at the polarization curve. These dendrites are fern-like shape (Figure 4a,f) constructed from very long stalk and side branches developed under a right angle from it (Figure 4b). The growth of the dendrites commences from one nucleation centre (Figure 4c), changing a direction of the growth very fast after the beginning of the growth, and terminating the growth by relatively sharp tips (Figure 4d,e). It is necessary to note that these dendrites are not oriented by their tips towards the bulk of the electrolyte, but they were oriented almost parallel with the electrode surface area and positioned very close to it. The change in dendrite growth direction can be attributed to the softness of tin as one of the authentic characteristics of tin [40]. Namely, tin is a very soft metal with a hardness of 1.5 at the Mohs scale of hardness of metals [41]. In these dendrites, the stalk and branches were in one plane pointing out the 2D (two-dimensional) character of the dendrites. Wranglen [42] denoted these branches by primary (P) branches classifying this dendrite type as the 2D(P) dendrite. At the macro level, the dendrites formed at *E*

of −1270 and −1400 mV vs. Ag/AgCl were very similar to each other, with a difference that larger number of the fern-like dendrites was formed at *E* of −1400 mV vs. Ag/AgCl than at *E* of −1270 mV vs. Ag/AgCl due to larger nucleation rate at the former mentioned cathodic potential.

Finally, Figure 5 shows Sn dendrites electrodeposited at cathodic potentials of −1600 (Figure 5a,b) and −1800 mV vs. Ag/AgCl (Figure 5c–e) situated to Part (III) at the polarization curve. At the first sight, it can be noted that they had somewhat different shapes from those obtained at the lower cathodic potentials. The intertwined network of the dendritic forms was obtained at both cathodic potentials (Figure 5a,c). The careful analysis of these dendrites revealed that they grew from one nucleation centre in three or more directions (Figure 5b,e). Each of the branches consisted of stalk and primary branches (the 2D(P) type). In the growth process, these dendrites can obtain a stem-like appearance (Figure 5d).

Morphology of Sn deposits obtained under galvanostatic conditions of the electrodeposition at a current density of −3 mA cm^{-2} is shown in Figure 6. The dendrites of various degree of ramification and shape, starting from a spear-like (Figure 6a) to very branchy 2D dendrites (Figure 6b–d), were obtained at this current density. The branches were a prismatic shape, as presented in Figure 6c,d, showing details of the dendrite from Figure 6b. It is necessary to note that during the growth process a spear-like dendrite (Figure 6a) was developed from the 2D dendrite consisting of stalk and primary branches. Certainly, the formation of all these diverse morphological forms will be discussed later.

(**a**)   (**b**)   (**c**)

(**d**)

Figure 6. Morphology of tin deposits electrodeposited at a current density of −3 mA cm^{-2} with an amount of the electricity of 400 mC. (**a**) spear-like, and (**b**–**d**) very branchy 2D dendrites.

3.3. Structural Analysis of Sn Dendritic Particles Obtained under Various Electrodeposition Conditions

The XRD patterns obtained for tin particles produced at various cathodic potentials (−1200, −1400 and −1800 mV vs. Ag/AgCl), at a current density of –3 mA cm^{-2}, as well as JCPDS standard No. 04-0673 for Sn are shown in Figure 7. The selected cathodic potentials belonged to Parts (I), (II) and (III) at the polarization curve. The recorded XRD patterns of Sn particles confirm that tin crystallizes in the body-centered tetragonal type of crystal lattice [2].
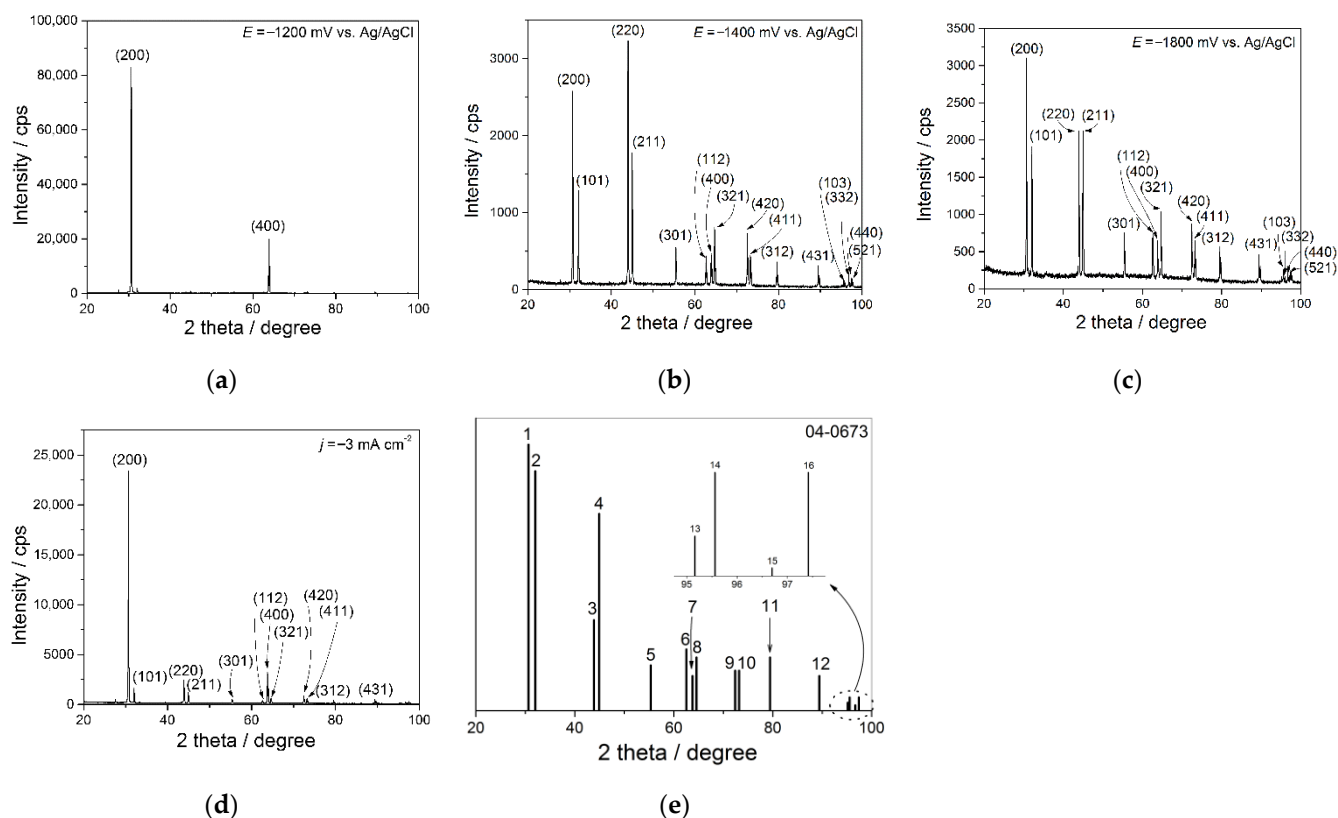
Figure 7. The XRD patterns of Sn powder particles obtained at cathodic potentials (*E*) of: (**a**) −1200 mV vs. Ag/AgCl, (**b**) −1400 mV vs. Ag/AgCl, (**c**) −1800 mV vs. Ag/AgCl, current density (*j*) of: (**d**) −3 mA cm^{-2}, and (**e**) Sn standard (04–0673): 1–(200), 2–(101), 3–(220), 4–(211), 5–(301), 6–(112), 7–(400), 8–(321), 9–(420), 10–(411), 11–(312), 12–(431), 13–(103), 14–(332), 15–(440), and 16–(521) crystal planes.

The XRD analysis of Sn particles showed that the needle-like and the spear-like dendrites obtained at −1200 mV vs. Ag/AgCl represented monocrystals of (200) and (400) orientation (Figure 7a). The high ratio of Sn crystallites oriented in these crystal planes also showed Sn dendritic particles produced galvanostatically at −3 mA cm^{-2} (Figure 7d). Aside from a dominant orientation of Sn crystallites in (200) and (400) crystal planes, these particles also showed a certain orientation of Sn crystallites in some other crystal planes.

The existence of very intensive various diffraction peaks in the XRD patterns obtained for Sn powders synthesized at −1400 and −1800 mV vs. Ag/AgCl (Figure 7b,c, respectively) demanded a more precise estimation of the preferred orientation of these Sn particles. For that purpose, a procedure based on a determination of "Texture Coefficients" (*TC*(*hkl*)) and "Relative Texture Coefficients" (*RTC*(*hkl*)) was applied [32–35]. The values *TC* and *RTC* coefficients, as well as the values of intensity of diffraction peaks (*R*(*hkl*)) for Sn particles obtained at cathodic potentials of −1400 and −1800 mV vs. Ag/AgCl, as well as for those obtained at a current density of −3 mA cm^{-2} are given in Table 1. In the examined 2*θ* range between 20 and 100°, sixteen main diffraction intensities (or peaks) of Sn are situated, indicating that the values of *RTC* coefficients larger than 6.25% indicate the existence of the preferred orientation in the particles. Simultaneously, the *TC* values larger than 1 indicate the existence of the preferred orientation [32].

Table 1. Texture calculations for Sn powder particles produced potentiostatically at cathodic potentials (*E*) of −1400 and −1800 mV vs. Ag/AgCl and galvanostatically at *j* of −3.0 mA cm^{-2} (1400—*E* = −1400 mV vs. Ag/AgCl; 1800—*E* = −1800 mV vs. Ag/AgCl; 3.0—*j* = −3.0 mA cm^{-2}; s—Sn standard). *R*—Intensity of the diffraction peak, *TC*—Texture Coefficient, and *RTC*—Relative Texture Coefficient.

Plane (*hkl*)	*R* (in %)			*R*$_s$ (in %)	*TC*			*RTC* (in %)		
	R$_{1400}$	*R*$_{1800}$	*R*$_{3.00}$		*TC*$_{1400}$	*TC*$_{1800}$	*TC*$_{3.00}$	*RTC*$_{1400}$	*RTC*$_{1800}$	*RTC*$_{3.00}$
(200)	20.0	19.5	64.3	22.2	0.90	0.88	2.89	4.60	4.13	22.1
(101)	10.0	12.0	4.49	20.0	0.50	0.600	0.22	2.55	2.82	1.72
(220)	25.0	13.4	6.76	7.57	3.30	1.77	0.89	16.9	8.32	6.85
(211)	9.12	13.4	3.23	16.5	0.55	0.81	0.20	2.81	3.81	1.50
(301)	4.28	4.73	1.34	3.79	1.13	1.25	0.35	5.77	5.87	2.71
(112)	3.38	4.66	1.05	5.12	0.66	0.91	0.20	3.37	4.28	1.57
(400)	3.62	4.06	8.92	2.90	1.25	1.40	3.08	6.39	6.58	23.6
(321)	6.26	6.51	1.71	4.45	1.41	1.46	0.38	7.20	6.86	2.94
(420)	5.67	5.52	2.35	3.34	1.70	1.65	0.70	8.69	7.75	5.40
(411)	3.50	4.07	1.62	3.34	1.05	1.22	0.48	5.37	5.73	3.72
(312)	2.80	3.61	1.14	4.45	0.63	0.81	0.26	3.21	3.81	1.96
(431)	2.40	2.92	0.85	2.90	0.83	1.01	0.29	4.23	4.75	2.25
(103)	0.50	1.03	0.38	0.67	0.75	1.54	0.57	3.82	7.24	4.40
(332)	1.04	1.63	0.43	1.11	0.94	1.47	0.39	4.79	6.91	2.99
(440)	1.31	1.37	0.62	0.44	2.94	3.08	1.40	15.0	14.5	10.7
(521)	1.15	1.58	0.80	1.11	1.04	1.42	0.72	5.32	6.67	5.50

Analysis of data given in Table 1 showed that Sn particles obtained at a current density of −3 mA cm^{-2} possessed the strong (200),(400) preferred orientation, and the weak (220),(440) preferred orientation. The fern-like dendrites produced at −1400 mV vs. Ag/AgCl showed the predominant (220),(440) preferred orientation, but also very weak (400),(321), and (420) preferred orientation. Finally, in Sn particles produced at −1800 mV vs. Ag/AgCl, Sn crystallites were oriented to a greater extent only in the (440) crystal plane. Aside from this plane, Sn particles also exhibited a weak (220),(400),(321),(420),(103),(332),(521) preferred orientation.

The values of the average size of Sn crystallites calculated from the XRD data were: 63.1, 77.4, and 70.5 nm for Sn dendritic particles produced at cathodic potentials of −1200, −1400, and −1800 mV vs. Ag/AgCl, respectively. The average crystallite size for galvanostatically synthesized Sn particles at −3 mA cm^{-2} was 90.3 nm. The obtained values clearly point out the nanostructural character of electrolytically synthesized Sn powders.

4. Discussion

The shape of the Sn polarization curve, characterized by an initial fast increase in the current density and by a relatively short plateau of the limiting diffusion current density of 100 mV, as well as the performed morphological analysis clearly confirms the belonging of tin to a group of so-called normal metals. The group of normal metals in the Winand classification of metals [43] is characterized by high values of both the exchange current density and overpotentials for hydrogen evolution reaction and by low melting point. The main characteristic of this metal group is the formation of irregular (powder) forms in the whole range of cathodic potentials and current densities, as shown here for Sn deposits.

Similar shapes of Sn polarization curves were also obtained from the citrate electrolytes [16], suggesting that these shapes represent the typical forms of the polarization curves characterizing Sn electrodeposition processes. He et al. [16] analyzed Sn electrolytes of various concentrations of both Sn(II) and citrate ions and the existence of maximum at the polarization curves attributed to the limiting diffusion current density (j_L) values. Considering the well-known fact that the limiting diffusion current density is related to the existence of the plateau of the limiting diffusion current density, it follows that Sn electrodeposition processes are characterized with two limiting diffusion current density values. The first j_L value is related to the maximum at the polarization curve, while the

second j_L value is related to the existence of a short, but well-defined plateau of the limiting diffusion current density.

Analysis of the morphology of Sn powders produced at the various cathodic potentials (Figures 3–5) offers a valuable explanation for this shape of the polarization curve. Namely, the formation of the long needle-like and the spear-like dendrites with the tips oriented to the bulk electrolyte (Figure 3) apparently increases the real surface area of the cathode, and as a result of it, a maximum at the polarization curve was observed. On the other hand, the fern-like dendrites were formed at the cathodic potential which corresponded to the plateau of the limiting diffusion current density (Figure 4a–d). These dendrites were positioned parallel and very close to the electrode surface, and in this case, the real electrode surface area was not significantly changed relative to the initial cathode surface area.

The part of the polarization curve characterized by the fast increase in the current density with increasing cathodic potential after the end of the plateau of the limiting diffusion current density represents another segment at the polarization curve for which the analysis of deserves special attention. This part can be attributed to vigorous hydrogen evolution, as in the case of copper [13,33,35,44], or to instantaneous formation and growth of dendrites, as in the case of silver [33,34], lead [45,46], and zinc [47]. Although the performed SEM analysis of Sn deposits revealed the positions originating from hydrogen evolution as a parallel reaction to Sn electrolysis (for example, see parts in circles in Figure 4g), the regular shapes of dendrites formed in the whole range of the cathodic potentials clearly indicate that this amount of generated hydrogen was not enough to achieve any significant effect on hydrodynamic conditions in the near-electrode layer, and hence, to inhibit tin dendritic growth.

Anyway, depending on the cathodic potential applied, the three kinds of Sn dendrites were formed: (a) needle-like and spear-like, (b) fern-like, and (c) stem-like dendrites formed by growth from one nucleation centre in more directions. The formation of all these dendritic forms can be explained by theories considering dendrite formation by electrolysis established by Diggle, Despić, Bockris [48] and supplemented by Popov et al. [13,49]. According to these theories, the origin of the dendrite is from a surface irregularity, denoted as a precursor of the dendrite, formed in the early stage of electrodeposition by growth from the initially formed nucleus, and placed deep inside the diffusion layer of the macro-electrode. The formation of dendrites by electrolysis processes is the diffusion-controlled process, thereby these theories especially point out a contribution of the spherical diffusion field to the final shape of metal dendrites. The radius of the spherical diffusion layer formed around the tip of every dendrite precursor is equal to the radius of the precursor. It can be shown by the application of these theories that the tips of the surface irregularities grow under the activation control, while simultaneously electrodeposition process to the flat part of the electrode surface occurs under the full diffusion control [13,48–50]. As a result of all these consecutive processes, dendrites of various shapes and ramifications are formed. Then, the fast rise in the current density with increasing the cathodic potential after the end of the plateau of the limiting diffusion current density can be attributed primarily to the activation-controlled growth at the tips of growing dendritic forms.

Aside from these main shapes of dendrites, well-defined crystal grains and fish bone-like structures were also formed. The well-defined crystal grains are formed at the same cathodic potential at which needle-like and spear-like dendrites were formed. Production of these morphological forms occurred at the very beginning of the diffusion control of electrodeposition, and it is also characteristic of the other metals from the group of normal metals like Pb [45] and Zn [47]. On the other hand, the fish bone-like structures represent a transitional form between needle-like and fern-like dendrites.

The morphology of Sn dendrites produced by the galvanostatic regime of electrolysis can be explained as follows. To the best of our knowledge, the dendrites with the branches of prismatic shape (Figure 6c,d) represent a novel type of Sn dendrites, not previously reported in the literature. Analysis of the chronopotentiometric curve shown in Figure 2d gives a reasonable explanation for the formation of all here shown galvanostatically synthesized

dendritic forms. The reached cathodic response after Sn electrodeposition at a current density of -3 mA cm^{-2} with an amount of the passed electricity of 400 mC was about -1200 mV vs. Ag/AgCl and less. The spear-like dendrites were formed as one of the shapes of dendrites at this current density (Figure 6a). In the potentiostatic mode, the spear-like dendrites are just formed at cathodic potentials of -1185 and -1200 mV vs. Ag/AgCl (Figure 3b,e). This is clear proof that the cathodic potential response controlled the morphology of electrolytically formed structures. The strong effect of the cathodic potential response on the morphology of Sn dendrites can also be seen by analysis of the growth of this spear-like dendrite. This dendrite commences a growth as the fern-like dendrite, in order to after a potential drop below a certain critical value its growth was transformed into the spear-like shape. As already shown, the fern-like dendrites are formed at higher cathodic potentials than the spear-like dendrites. The emergence of prismatic forms in the Sn dendrites is also proof of control of the electrodeposition process by the cathodic potential response. Namely, regular crystal grains like prisms are a characteristic of electrodeposition processes at lower cathodic potentials before an initiation of dendritic growth.

Aside from the strong effect on the morphology of Sn particles, the electrodeposition conditions also affected their structure. For tin crystal lattice, (110) plane, and hence, (220) and (440) planes, is crystal plane with the lowest surface energy [51]. Making analogy with metals belonging to the face-centered cubic (fcc) type of crystal lattice [52,53], it follows that electrodeposition rates on (110),(220) and (440) planes are smaller than those on other planes. For that reason, these planes can be denoted as slow-growing planes, and they survive the growth process by constructing the interior of both stalk and the branches in fern-like and stem-like dendrites. Hence, the orientation of crystallites in (220) and (440) planes originates from the growth centres situated in the interior of the growing dendrites. On the other hand, all other planes represent the fast-growing planes that disappear in the growth process. The orientation of crystallites in these planes originates from the growth centres at tips and angles of the growing dendrites. The larger ratio of Sn crystallites oriented in the fast-growing crystal planes in the stem-like dendrites produced at a cathodic potential of -1800 mV vs. Ag/AgCl than in the fern-like dendrites produced at -1400 mV vs. Ag/AgCl can be attributed to more branchy structure of the stem-like particles, i.e., larger number of the tips and the angles in these particles than in the fern-like dendrites.

Simultaneously, the needle-like and the spear-like dendrites represented monocrystals of (200),(400) preferred orientation. These particles are formed at lower cathodic potential (-1200 mV vs. Ag/AgCl) than the fern-like and stem-like dendritic particles. It is clear that at this cathodic potential, the electrodeposition rate on (200) and (400) crystal planes is enough low that these planes can survive the growth process, causing the formation of no branchy needle-like and spear-like dendrites.

5. Conclusions

Sn dendrites of various shapes were synthesized via an electrochemical route from the alkaline hydroxide electrolyte applying both potentiostatic and galvanostatic regimes of electrolysis. Morphological and structural characterization of the obtained particles was made by scanning electron microscopy (SEM) and by X-ray diffraction (XRD) techniques, respectively. Correlation among the polarization characteristics for this electrodeposition system, morphology, and structure of the Sn dendrites was considered with the aim to explain the formation of various dendritic forms. Based on the obtained results, it follows:

(a) The polarization curve for Sn electrodeposition from the alkaline electrolyte consisted of three parts. Every part was characterized by the specific shape of the dendrites. The first part is featured by the fast increase in the current density and then by its sharp decrease after reaching the maximum. The needle-like and the spear-like dendrites were predominately formed in this part. The second part is primarily characterized by relatively short plateau of the limiting diffusion current density. The fern-like dendrites are formed inside this part. The third part is characterized by the fast

increase of the current density with increasing the cathodic potential. The formation of the stem-like dendrites characterizes this part of the polarization curve.

(b) The novel type of Sn dendrites with branches of prismatic shape was formed by the galvanostatic regime of the electrodeposition.

(c) The structure of the Sn dendrites also strongly depended on the applied cathodic potential and the current density. The dendrites of the needle-like and the spear-like shape were monocrystals of (200) and (400) preferred orientation. The fern-like dendrites possessed the predominant (220) and (440) preferred orientation. The stem-like particles showed (440) preferred orientation, but with the increased ratio of Sn crystallites oriented in some other crystal planes.

(d) The XRD analysis of the Sn particles revealed that all types of dendritic particles were of nanostructural characteristics.

(e) Very diverse morphological forms obtained by various electrolysis processes clearly indicate that this method of powder synthesis represents a promising tool for obtaining Sn powders suitable for application in various technologies mentioned in the Introduction of this study.

Appendix A

Determination of the "Texture Coefficient", TC(hkl) and the "Relative Texture Coefficient", RTC(hkl) by Analysis of the XRD Data

The ratio of reflection intensity (*hkl*) to the sum of all intensities of the recorded reflections, *R*(*hkl*), (in %) is given by Equation (A1) [32,33]:

$$R(hkl) = \frac{I(hkl)}{\sum\limits_{i}^{16} I(h_i k_i l_i)} \times 100 \tag{A1}$$

where *I* (*hkl*) is a reflection intensity (*hkl*) plane, in cps, and $\sum\limits_{i}^{16} I(h_i k_i l_i)$ is the sum of all intensities of the recorded reflections, in cps, for the powder being considered (in the case of Sn, it is sixteen).

The "Texture Coefficient", *TC*(*hkl*), for every (*hkl*) reflection is defined by Equation (A2):

$$TC(hkl) = \frac{R(hkl)}{R_s(hkl)} \tag{A2}$$

where $R_s(hkl)$ is defined in the same way as given by Equation (A2), but is related to the standard for metal under consideration. This coefficient gives the accurate quantitative information about the absolute reflection intensity.

Finally, the "Relative Texture Coefficient", $RTC(hkl)$ is defined by Equation (A3):

$$RTC(hkl) = \frac{TC(hkl)}{\sum\limits_{i}^{16} TC(h_i k_i l_i)} \times 100 \tag{A3}$$

The $RTC\,(hkl)$ coefficient defines the reflection intensity (hkl) relative to the standard (included in the TC values).

References

1. Tin Powder—Production and Applications. Available online: https://nanografi.com/blog/tin-sn-powder/ (accessed on 3 June 2022).
2. Wang, Z.; Ru, J.; Hua, Y.; Bu, J.; Geng, X.; Zhang, W. Electrodeposition of Sn powders with pyramid chain and dendrite structures in deep eutectic solvent: Roles of current density and SnCl$_2$ concentration. *J. Solid State Electrochem.* **2021**, *25*, 1111–1120. [CrossRef]
3. Zhang, L.P.; Zhao, Y.Y. Particle size distribution of tin powder produced by centrifugal atomisation using rotating cups. *Powder Technol.* **2017**, *318*, 62–67. [CrossRef]
4. Chee, S.S.; Lee, J.H. Reduction Synthesis of Tin Nanoparticles Using Various Precursors and Melting Behavior. *Electron. Mater. Lett.* **2012**, *8*, 587–593. [CrossRef]
5. Zou, C.D.; Gao, Y.L.; Yang, B.; Zhai, Q.J. Size-dependent melting properties of Sn nanoparticles by chemical reduction synthesis. *Trans. Nonferrous Met. Soc. China* **2010**, *20*, 248–253. [CrossRef]
6. Chee, S.S.; Lee, J.H. Synthesis of tin nanoparticles through modified polyol process and effects of centrifuging and drying on nanoparticles. *Trans. Nonferrous Met. Soc. China* **2012**, *22*, 707–711. [CrossRef]
7. Qiu, L.; Pol, V.G.; Calderon-Moreno, J.; Gedanken, A. Synthesis of tin nanorods via a sonochemical method combined with a polyol process. *Ultrason. Sonochem.* **2005**, *12*, 243–247. [CrossRef]
8. Dong, J.; Wu, F.; Han, Q.; Qi, J.; Gao, W.; Wang, Y.; Li, T.; Yang, Y.; Sun, M. Electrochemical synthesis of tin plasmonic dendritic nanostructures with SEF capability through in situ replacement. *RSC Adv.* **2020**, *10*, 36042–36050. [CrossRef]
9. Popov, K.I.; Pavlović, M.G.; Jovićević, J.N. Morphology of tin powder particles obtained in electrodeposition on copper cathode by constant and square-wave pulsating overpotential from Sn(II) alkaline solution. *Hydrometallurgy* **1989**, *23*, 127–137. [CrossRef]
10. Kim, T.H.; Hong, K.S.; Sohn, D.R.; Kim, M.J.; Nam, D.H.; Cho, E.A.; Kwon, H.S. One-step synthesis of multilayered 2D Sn nanodendrites as a high-performance anode material for Na-ion batteries. *J. Mater. Chem. A* **2017**, *5*, 20304–20315. [CrossRef]
11. Wang, Z.; Ru, J.; Hua, Y.; Wang, D.; Bu, J. Morphology-Controlled Preparation of Sn Powders by Electrodeposition in Deep Eutectic Solvent as Anodes for Lithium Ion Batteries. *J. Electrochem. Soc.* **2020**, *167*, 082504. [CrossRef]
12. Amiri, M.; Nouhi, S.; Azizian-Kalandaragh, Y. Facile Synthesis of Silver Nanostructures by Using Various Deposition Potential and Time: A Nonenzymetic Sensor For Hydrogen. *Mater. Chem. Phys.* **2015**, *155*, 129–135. [CrossRef]
13. Popov, K.I.; Djokić, S.S.; Nikolić, N.D.; Jović, V.D. *Morphology of Electrochemically and Chemically Deposited Metals*; Springer: New York, NY, USA, 2016; pp. 1–368. [CrossRef]
14. Rudnik, E.; Włoch, G. Studies on the electrodeposition of tin from acidic chloride–gluconate solutions. *App. Surf. Sci.* **2013**, *265*, 839–849. [CrossRef]
15. Rudnik, E. Effect of anions on the electrodeposition of tin from acidic gluconate baths. *Ionics* **2013**, *19*, 1047–1059. [CrossRef]
16. He, A.; Liu, Q.; Ivey, D.G. Electrodeposition of tin: A simple approach. *J. Mater. Sci. Mater. Electron.* **2008**, *19*, 553–562. [CrossRef]
17. Shin, H.C.; Dong, J.; Liu, M. Nanoporous Structures Prepared by an Electrochemical Deposition Process. *Adv. Mater.* **2003**, *15*, 1610–1614. [CrossRef]
18. Khabazian, S.; Sanjabi, S.; Tonti, D. Electrochemical growth of two-dimensional tin nano-platelet as high-performance anode material in lithium-ion batteries. *J. Ind. Eng. Chem.* **2020**, *84*, 120–130. [CrossRef]
19. Azpeitia, L.A.; Gervasi, C.A.; Bolzan, A.E. Electrochemical aspects of tin electrodeposition on copper in acid solutions. *Electrochim. Acta* **2019**, *298*, 400–412. [CrossRef]
20. Low, C.T.J.; Walsh, F.C. The influence of a perfluorinated cationic surfactant on the electrodeposition of tin from a methanesulfonic acid bath. *J. Electroanal. Chem.* **2008**, *615*, 91–102. [CrossRef]
21. Orhan, G.; Gezgin, G.G. Response surface modeling and evaluation of the influence of deposition parameters on the electrolytic Cu-Sn alloy powders production. *Metall. Mater. Trans. B* **2011**, *42*, 771–782. [CrossRef]
22. Ignatova, K.; Popov, I. Structure and electrocatalytic ability of Sn–Ni alloy powders prepared by direct and pulse electrodeposition. *Mater. Chem. Phys.* **2021**, *263*, 124410. [CrossRef]
23. Walsh, F.C.; Low, C.T.J. A review of developments in the electrodeposition of tin. *Surf. Coat. Technol.* **2016**, *288*, 79–94. [CrossRef]

24. Lodge, A.W.; Hasan, M.M.; Bartlett, P.N.; Beanland, R.; Hector, A.L.; Kashtiban, R.J.; Levason, W.; Reid, G.; Sloan, J.; Smith, D.C.; et al. Electrodeposition of tin nanowires from a dichloromethane based electrolyte. *RSC Adv.* **2018**, *8*, 24013–24020. [CrossRef] [PubMed]

25. Cao, X.; Xu, L.; Wang, C.; Li, S.; Wu, D.; Shi, Y.; Liu, F.; Xue, X. Electrochemical Behavior and Electrodeposition of Sn Coating from Choline Chloride–Urea Deep Eutectic Solvents. *Coatings* **2020**, *10*, 1154. [CrossRef]

26. Ghosh, S.; Roy, S. Characterization of tin films synthesized from ethaline deep eutectic solvent. *Mater. Sci. Eng. B* **2014**, *190*, 104–110. [CrossRef]

27. Wang, Z.; Cheng, M.; Bu, J.; Cheng, L.; Ru, J.; Hua, Y.; Wang, D. Understanding the electrochemical behavior of Sn (II) in choline chloride-ethylene glycol deep eutectic solvent for tin powders preparation. *Adv. Powder Technol.* **2022**, *33*, 103670. [CrossRef]

28. Liu, D.; Groult, H.; Gaillon, L.; Rizzi, C.; Soulmi, N.; Julien, C.M.; Briot, E.; Krulic, D. Tunable electrodeposition of Sn and Sn-based alloys using ionic liquids. *J. Solid State Electrochem.* **2015**, *19*, 2517–2532. [CrossRef]

29. Hsu, C.H.; Yang, C.H.; Wang, Y.C.; Chang, J.K. Nanostructured tin electrodeposited in ionic liquid for use as an anode for Li-ion batteries. *J. Mater. Chem. A* **2014**, *2*, 16547–16553. [CrossRef]

30. Lipkin, V.M.; Fesenko, L.N.; Lipkin, S.M. Tin Powders Electrodeposition from Choline Chloride Based Ionic Liquid. *Solid State Phenom.* **2018**, *284*, 1252–1256. [CrossRef]

31. Lipkin, M.S.; Yalyushev, N.I.; Lipkin, V.M.; Burakov, M.A.; Semenkova, A.V.; Kuznetsov, D.N.; Bachayev, R.M.; Novoselov, V.V. Studies on the Reversibility of Electrolytic Tin Powder Obtained from an Ionic Liquid. *Inorg. Mater. Appl. Res.* **2021**, *12*, 504–508. [CrossRef]

32. Berube, L.P.; Esperance, G.L. A Quantitative Method of Determining of the Degree of Texture of Zinc Electrodeposits. *J. Electrochem. Soc.* **1989**, *136*, 2314–2315. [CrossRef]

33. Nikolić, N.D.; Maksimović, V.M.; Avramović, L.J. Correlation of Morphology and Crystal Structure of Metal Powders Produced by Electrolysis Processes. *Metals* **2021**, *11*, 859. [CrossRef]

34. Avramović, L.; Pavlović, M.M.; Maksimović, V.M.; Vuković, M.; Stevanović, J.S.; Bugarin, M.; Nikolić, N.D. Comparative Morphological and Crystallographic Analysis of Electrochemically- and Chemically-Produced Silver Powder Particles. *Metals* **2017**, *7*, 160. [CrossRef]

35. Avramović, L.; Maksimović, V.M.; Baščarević, Z.; Ignjatović, N.; Bugarin, M.; Marković, R.; Nikolić, N.D. Influence of the Shape of Copper Powder Particles on the Crystal Structure and Some Decisive Characteristics of the Metal Powders. *Metals* **2019**, *9*, 56. [CrossRef]

36. Suryanarayana, C.; Norton, M.G. *X-Ray Diffraction, A Practical Approach*; Springer: New York, NY, USA, 1998.

37. Jović, V.D.; Jović, B.M.; Pavlović, M.G. Electrodeposition of Ni, Co and Ni–Co alloy powders. *Electrochim. Acta* **2006**, *51*, 5468–5477. [CrossRef]

38. Nikolić, N.D.; Živković, P.M.; Pavlović, M.G.; Baščarević, Z. Overpotential controls a morphology of electrolytically produced copper dendritic forms. *J. Serb. Chem. Soc.* **2019**, *84*, 1209–1220. [CrossRef]

39. Popov, K.I.; Pavlović, M.G.; Maksimović, M.D.; Krstajić, S. The comparison of galvanostatic and potentiostatic copper powder deposition on platinum and aluminium electrodes. *J. Appl. Electrochem.* **1978**, *8*, 503–514. [CrossRef]

40. Lowenheim, F.A. (Ed.) *Modern Electroplating*, 3rd ed.; John Wiley & Sons, Inc.: New York, NY, USA, 1974.

41. The Mohs Scale of Hardness for Metals: Why It Is Important. Available online: https://www.jewelrynotes.com/the-mohs-scale-of-hardness-for-metals-why-it-is-important/ (accessed on 3 June 2022).

42. Wranglen, G. Dendrites and Growth Layers in the Electrocrystallization of Metals. *Electrochim. Acta* **1960**, *2*, 130–146. [CrossRef]

43. Winand, R. Electrodeposition of Metals and Alloys–New Results and Perspectives. *Electrochim. Acta* **1994**, *39*, 1091–1105. [CrossRef]

44. Nikolić, N.D.; Popov, K.I.; Pavlović, L.J.; Pavlović, M.G. The Effect of Hydrogen Codeposition on the Morphology of Copper Electrodeposits. I. The Concept of Effective Overpotential. *J. Electroanal. Chem.* **2006**, *588*, 88–98. [CrossRef]

45. Nikolić, N.D.; Popov, K.I.; Živković, P.M.; Branković, G. A New Insight into the Mechanism of Lead Electrodeposition: Ohmic–diffusion Control of the Electrodeposition Process. *J. Electroanal. Chem.* **2013**, *691*, 66–76. [CrossRef]

46. Nikolić, N.D. Influence of the Exchange Current Density and Overpotential for Hydrogen Evolution Reaction on the Shape of Electrolytically Produced Disperse Forms. *J. Electrochem. Sci. Eng.* **2020**, *10*, 111–126. [CrossRef]

47. Nikolić, N.D.; Živković, P.M.; Lović, J.D.; Branković, G. Application of the general theory of disperse deposits formation in an investigation of mechanism of zinc electrodeposition from the alkaline electrolytes. *J. Electroanal. Chem.* **2017**, *785*, 65–74. [CrossRef]

48. Diggle, J.W.; Despic, A.R.; Bockris, J.O.M. The Mechanism of the Dendritic Electrocrystallization of Zinc. *J. Electrochem. Soc.* **1969**, *116*, 1503–1514. [CrossRef]

49. Popov, K.I.; Nikolić, N.D. General Theory of Disperse Metal Electrodeposits Formation. In *Electrochemical Production of Metal Powders (Modern Aspects of Electrochemistry)*; Djokić, S.S., Ed.; Springer International Publishing: New York, NY, USA, 2012; pp. 1–62.

50. Despić, A.R.; Popov, K.I. Transport controlled deposition and dissolution of metals. In *Modern Aspect of Electrochemistry, No. 7*; Conway, B.E., Bockris, J.O.M., Eds.; Plenum Press: New York, NY, USA, 1972; pp. 199–313.

51. Wang, S.G.; Tian, E.K.; Lung, C.W. Surface Energy of Arbitrary Crystal Plane of bcc and fcc Metals. *J. Phys. Chem. Solids* **2000**, *61*, 1295–1300. [CrossRef]

52. Bockris, J.O.M.; Reddy, A.K.N.; Gamboa-Aldeco, M.E. *Modern Electrochemistry 2A, Fundamentals of Electrodics*; Kluwer Academic/Plenum Publishers: New York, NY, USA; Springer: Boston, MA, USA, 2000; p. 1333.

53. Nikolić, N.D.; Maksimović, V.M.; Branković, G. Morphological and Crystallographic Characteristics of Electrodeposited Lead from the Concentrated Electrolyte. *RSC Adv.* **2013**, *3*, 7466–7471. [CrossRef]